2D and 3D Millimeter-Wave Synthetic Aperture Radar Imaging on a PR2 Platform

Claire M. Watts[1], Patrick Lancaster[2], Andreas Pedross-Engel[1], Joshua R. Smith[1,2], and Matthew S. Reynolds[1,2]

***Abstract*— Optical depth cameras, including both time-of-flight and structured-light sensors, have led to dramatic improvements in robot sensing and perception. We propose the use of millimeter-wave (mmW) radar as an important complement to optical sensors. While the millimeter wavelengths of radar sensors do not support as high resolution as the nanometer wavelength of optical sensors, the ability of mmW signals to penetrate smoky and foggy environments as well as see through many opaque objects makes them a compelling sensor for navigation as well as manipulation in challenging environments. We present a series of 2D and 3D mmW images made with a hand-held antenna grasped by a PR2 robot. The radar image sensor uses a mechanical "painting" motion to acquire multiple views of the target object over the 15 − 26.5 GHz K-band. A GPU-based reconstruction algorithm synthesizes 2D and 3D images of the target object. We demonstrate a ground range resolution of 13.6 mm and a cross-range resolution of 7.1 mm for objects up to 0.5 m away from the robot. We further demonstrate imaging objects through fog, as well as through opaque paper.**

I. Introduction

Radar imaging systems have their roots in military sensing applications and were developed during World War II [1]. Radar is still an essential sensing technology today, and has increasing potential to augment widely-used optical sensors such as depth cameras and lidar in challenging environments.

Millimeter wave (mmW) imaging can augment optical systems by overcoming some of their fundamental limitations, such as nighttime imaging, sensing over long distances, and even imaging in adverse weather such as rain and fog [2]. Mobile autonomous systems could benefit greatly from mmW imaging for navigation. For example, the lidar systems currently mounted on many self-driving cars have trouble operating in heavy rain [3]. The integration of a mmW imager into an autonomous vehicle would pave the way for all-weather operation.

Current technology for robot navigation includes optical cameras, sonar [4], laser range finders [5], and structured light such as the Microsoft Kinect [6]. In addition to adding improved resolution to sonar sensing systems, millimeter wave imaging could also greatly expand the utility of robotic systems operating in hazardous environments, such as in a smoke-filled building, or in other environments where threat objects may be concealed from optical view. For example, there has been significant investment in robots to seek out land mines, where navigating dangerous obscured threats is essential [7].

In this work, we demonstrate synthetic aperture radar (SAR) imaging with K-band (15 − 26.5 GHz) antennas mounted on a PR2 robot. The robot arm allows the antennas to be moved with 7 degrees of freedom to gather multiple views of a scene that can be coherently reconstructed to form 2D and 3D images. In addition, we demonstrate the capability of mmW imaging through various impairments that optical cameras cannot penetrate, such as opaque coverings and fog. We show that K-band SAR images add a new imaging capability for sensing and perception in autonomous robotic systems.

II. Related Work

While SAR imaging for mobile robot navigation has been previously demonstrated, factors have prevented systems from achieving the resolution we achieve here, which is closer to optical images. Ultra wideband imaging systems have typically given limited resolution, on the order of meters, due to their long operation wavelength [8]. In addition, current systems that operate at shorter wavelengths, into the millimeter wave regime, have narrow bandwidths on the order of a few hundred MHz, also limiting their resolution [9], [10]. We are able to image smaller and more complex objects than similar robotic SAR systems through the use of both high frequency millimeter waves and a much wider bandwidth of over 10 GHz, yielding range resolution on the order of 10 mm. In addition, this work is not limited to sensing objects that have been previously tagged, as is the case when localizing RFID tagged objects [11], [12]. The approach presented here allows for imaging of arbitrary scenes with unknown objects, as long as the objects have reflectivity in the mmW band.

III. Overview of SAR Imaging

A. Basic SAR Mechanism

Radar (radio detection and ranging) imaging transmits electromagnetic radiation onto a scene and uses the backscattered signal to gain information about the reflectivity profile of the scene [1]. Often, chirps (compressed high intensity

[1]Claire M. Watts, Andreas Pedross-Engel, Joshua R. Smith, and Matthew S. Reynolds are with the Department of Electrical Engineering, University of Washington, Seattle, WA 98105, USA wattsc2@uw.edu, pedross@uw.edu, jrs@cs.washington.edu, matt.reynolds@ee.washington.edu

[2]Patrick Lancaster, Joshua R. Smith, and Matthew S. Reynolds are with the Department of Computer Science and Engineering, University of Washington, Seattle, WA 98105, USA planc509@cs.washington.edu

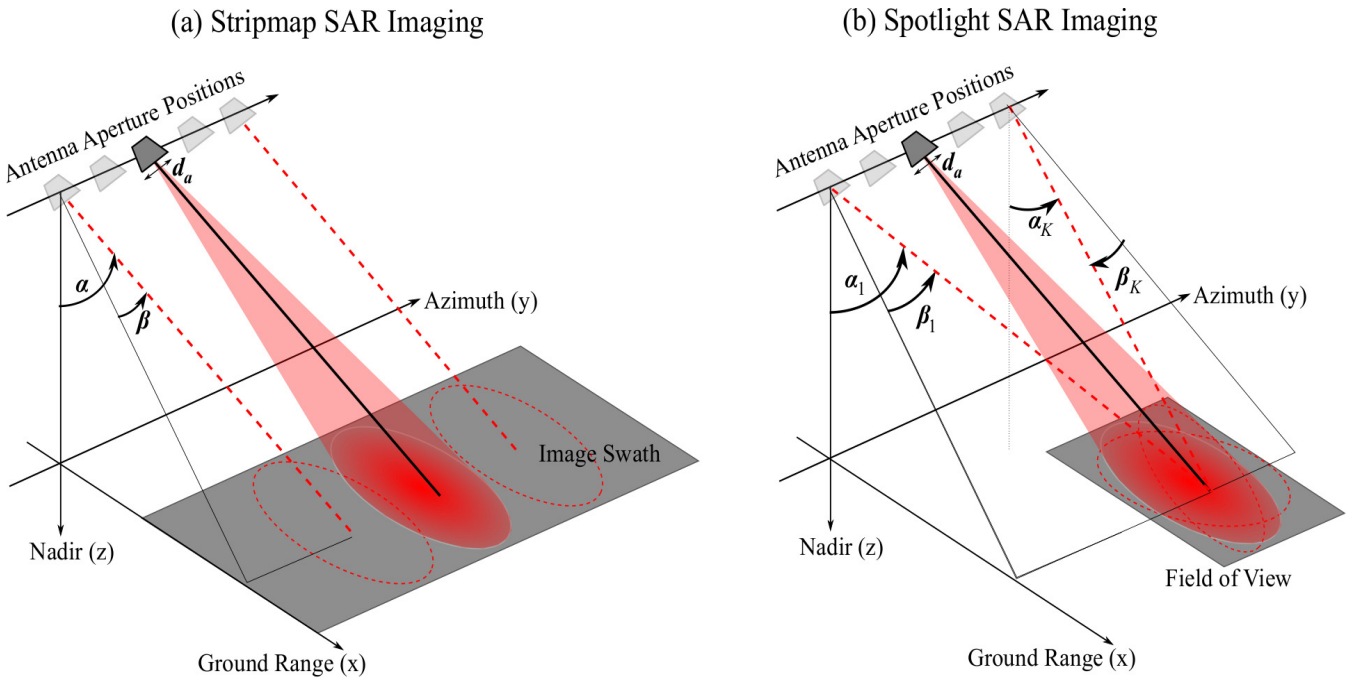

Fig. 1. Conceptual schematic of synthetic aperture radar imaging using an antenna with an aperture d_{a}. (a) Stripmap imaging with a fixed squint angle, β and looking angle, α. (b) Spotlight imaging - the antenna beam is steered with variable squint angles, $\beta = [\beta_1, ..., \beta_K]$, and looking angles, $\alpha = [\alpha_1, ..., \alpha_K]$, in order to constantly illuminate a single area.

radar pulses), in which the frequency linearly changes over some time period T, are used as the transmit waveform [13]. Radar images are usually assumed to be comprised of a dense array of point scatterers. Range information for some scattering point in the scene is determined from the time delay of the backscattered signal via cross-correlation of the transmitted and received waveforms. The range resolution δ_{r}, given as

$$\delta_{\mathrm{r}} = \frac{c_0}{2B}, \tag{1}$$

is proportional to the period of the chirp, T, or inversely proportional to the frequency bandwidth, B, where c_0 denotes the speed of light [1].

By moving the radar antenna, another dimension of information is gained (called the cross-range or azimuth dimension) and is determined by the placement of the antenna beam footprint. Hence, the azimuth resolution δ_{a}, given as

$$\delta_{\mathrm{a}} = \frac{\lambda}{d_{\mathrm{a}}} r_0, \tag{2}$$

of these systems is set by the beamwidth of the antenna [13]. Here, λ is the wavelength of operation, d_{a} is the antenna aperture size, and r_0 is the range distance to the target.

B. Benefits of SAR Imaging over Conventional Radar Imaging

Synthetic aperture radar imaging is a method which uses the motion of an antenna to increase the antennas's effective aperture beyond the antenna's physical size, and hence improves image resolution. SAR imaging has widespread use in airborne and spaceborne systems, for example to observe physical properties of the earth, monitor disaster sites, and detect man-made targets [1].

SAR imaging uses the Doppler shift of backscattered pulses to determine the cross range position of point scatterers in the scene. The cross-range resolution is based on the Doppler resolution of the system, and is therefore proportional to the time a point in the scene is exposed to the antenna beam. Thus, in SAR systems $\delta_{\mathrm{a,SAR}}$ is inversely proportional to the length of the synthetic aperture (L_{SA}), which again is inversely proportional to the size of the antenna [13], so that

$$\delta_{\mathrm{a,SAR}} = \frac{\lambda}{2L_{\mathrm{SA}}} r_0 = \frac{d_{\mathrm{a}}}{2}. \tag{3}$$

By moving the antenna, a large antenna aperture is synthesized without the size and weight burden that would come from having extremely large physical antennas.

C. SAR Imaging Geometry

Fig. 1 shows a conceptual schematic of a SAR imaging system. Transmitted and received power can come from the same source (monostatic SAR) or different sources (bistatic or multistatic SAR). For a 1D scan of a scene (producing a 2D image), the antenna moves along the azimuth dimension and emits radiation in the range dimension, towards the imaged scene. The direction perpendicular to the antenna motion along the plane of the imaging scene is the ground range dimension. The antenna can be oriented at some angle with respect to the nadir (the looking angle, α) or the range vector (the squint angle, β). The looking angle will affect

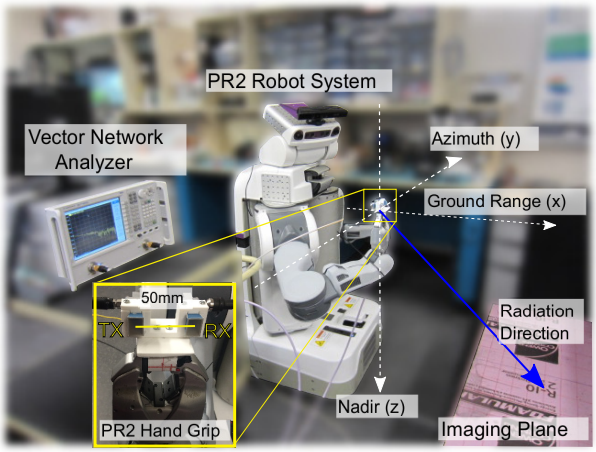

Fig. 2. Photograph of SAR imaging set up with key components labeled. The inset shows the antennas mounted in the grip of the PR2.

the resolution δ_{gr} of the ground range, which is given as

$$\delta_{\text{gr}} = \frac{\delta_{\text{r}}}{\sin\alpha}. \tag{4}$$

D. Modalities of SAR Imaging

There are several methods of SAR imaging that are useful for different purposes. Two of the most common types are called stripmap SAR and spotlight SAR. Fig. 1 details the main difference between these two processes. Stripmap (Fig. 1a) imaging fixes the looking angle and the squint angle, mapping out a swath as the antenna moves. In contrast, spotlight imaging (Fig. 1b) changes the radiation direction of the antenna to illuminate a single area while the antenna moves. While spotlight imaging restricts the image size, the resolution in the azimuth dimension can be increased over stripmap imaging [13].

E. Reconstructing SAR Images

When reconstructing SAR images from measured signals, it is assumed that the region of interest (ROI) can be approximated by a uniform grid of point targets each with a complex reflectivity. The SAR hardware collects a number of transmitter/receiver position dependent transfer functions. These transfer functions encode the position and reflectivity of each point target comprising the region of interest. In most cases, the equivalent impulse response is obtained from a variant of cross-correlation of the received signal with the transmitted signal.

The equivalent discrete (sampled) frequency response vector $\mathbf{y}_k$ at SAR system position $k \in \{1,\ldots,K\}$ of the ROI can also be directly measured using a vector network analyzer, as we have done in our laboratory imaging measurements.

Assuming a scene consisting of M hypothetical point scatterers, the l-th discretely sampled frequency point of the measurement vector $\mathbf{y}_k$ is given as

$$y_{k,l} = \sum_{m\in M} \rho_m \alpha_{k,l,m} e^{-j\omega_l \frac{R\left(\mathbf{x}_k^{TX},\mathbf{x}_k^{RX},\mathbf{x}_m\right)}{c_0}} + \nu_{k,l}, \tag{5}$$

where ρ_m is the complex reflection coefficient of the m-th point scatterer, $\alpha_{k,l,m}$ is the propagation channel including path loss and antenna response, ω_l is the angular frequency of interest, and $\nu_{k,l}$ is measurement noise. Note that $R\left(\mathbf{x}_k^{TX},\mathbf{x}_k^{RX},\mathbf{x}_m\right)$ denotes the distance between the m-th point scatterer and the positions of the antennas at the k-th measurement position, hence

$$R\left(\mathbf{x}_k^{TX},\mathbf{x}_k^{RX},\mathbf{x}_m\right) = ||\mathbf{x}_k^{TX} - \mathbf{x}_m|| + ||\mathbf{x}_k^{RX} - \mathbf{x}_m||, \tag{6}$$

where $\mathbf{x}_k^{TX}$ is the k-th position of the transmit antenna phase center, $\mathbf{x}_k^{RX}$ is the k-th position of the receive antenna phase center, $\mathbf{x}_m$ is the position of m-th point scatterer as determined by the defined reconstruction grid, and $||\mathbf{x}||$ denotes the norm of the vector $\mathbf{x}$.

Concatenating all K measurements gives

$$\mathbf{y} = \mathbf{H}\boldsymbol{\rho} + \boldsymbol{\nu} \tag{7}$$

where $\mathbf{y} = \left[\mathbf{y}_1^T \ldots \mathbf{y}_K^T\right]^T$, $\boldsymbol{\rho} = \left[\rho_1 \ldots \rho_M\right]^T$, $\boldsymbol{\nu}$ is measurement noise, and $(.)^T$ is the transpose operator. The measurement matrix $\mathbf{H}$ gives the dependence between the point scatterers and each measurement.

SAR reconstruction is the solution of the inverse problem defined in (7) to obtain an estimate of the reflection coefficients $\hat{\boldsymbol{\rho}}$ from the measurements $\mathbf{y}$, hence

$$\hat{\boldsymbol{\rho}} = \mathbf{A}\mathbf{y} \tag{8}$$

where $\mathbf{A}$ is the reconstruction matrix. As $\mathbf{H}$ is in many cases ill-conditioned, obtaining $\hat{\boldsymbol{\rho}}$ by multiplying $\mathbf{y}$ with e.g. the Moore-Penrose pseudo inverse $\mathbf{A} = \left(\mathbf{H}^\dagger\mathbf{H}\right)^{-1}\mathbf{H}^\dagger$ [14] gives an unstable solution, where $(.)^\dagger$ denotes the complex-transpose operator. An alternative, which is used in this work, is to define $\mathbf{A} = \mathbf{H}^\dagger$ [1], [15], i.e. the matched filter reconstruction algorithm. To improve computation time we implemented this algorithm using Nvidia CUDA, a parallel computing platform and application programming interface [16].

F. PR2 Robot System

The radar antenna module is actuated by the PR2, shown in Fig. 2, a highly versatile robot created by Willow Garage for mobile manipulation research. The PR2's ability to serve as a hardware platform for a wide variety of manipulation tasks is facilitated by its two 7-degree-of-freedom arms. Given a kinematically favorable goal position, the PR2 is typically capable of moving the specified end effector to within half of a centimeter of that goal. The PR2's two end effectors take the form of parallel jaw grippers whose fingertips can be fitted with pressure, optical, electric field and other types of sensors in order to gather geometric, surface, and other properties of an object of interest at close range. The PR2 can also utilize head-mounted cameras, including the Microsoft Kinect, to perceive the surrounding

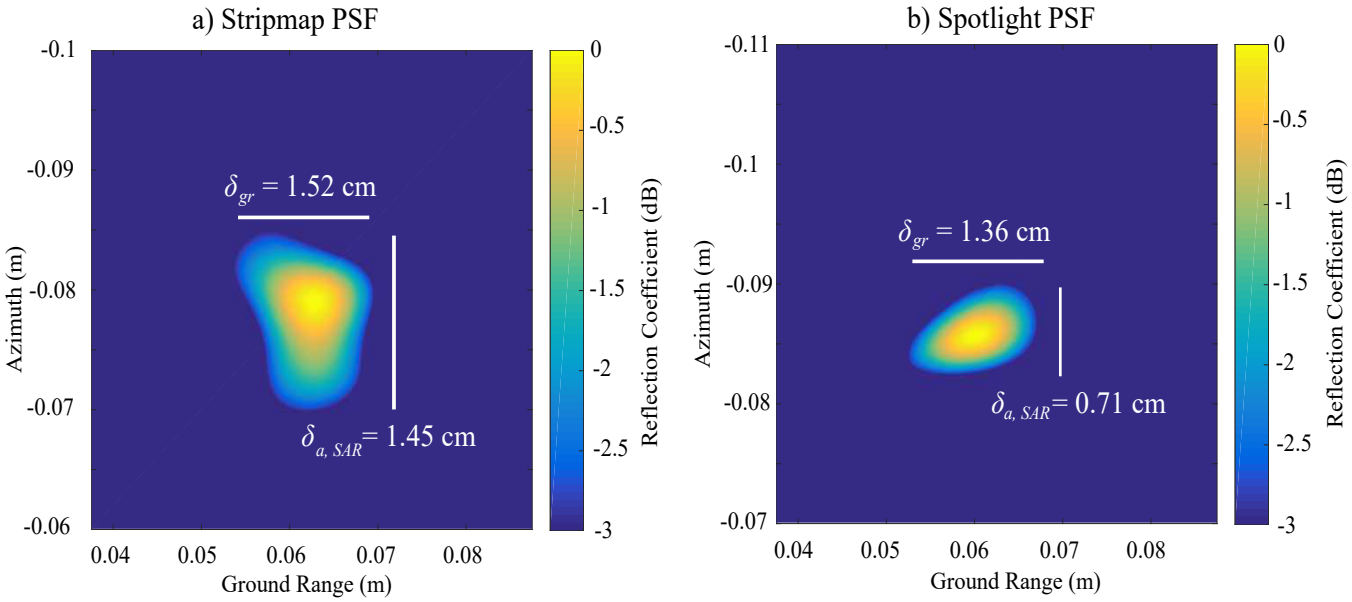

Fig. 3. (a) Stripmap and (b) spotlight images of point sources. Point spread functions display ground range and azimuth resolution.

environment. Two quad core i7 Xeon Processors in the base of the robot provide the computational power necessary to drive each of the PR2s modules [17].

G. Antenna System

We have outfitted the PR2 with bistatic antennas for SAR imaging. The antennas are 10 dB standard gain horn antennas with beamwidths in the E-field and H-field dimensions of 58° and 57° respectively [18]. The antenna has physical dimensions of $d_\mathrm{a} = 13.2$ mm in the azimuth dimension. The transmit and receive antennas are mounted approximately 50 mm apart, as shown in the inset of Fig. 2.

We use an Agilent A5222N network analyzer as the source and receiver. The cables have been calibrated out of the measurement with a full 2 port calibration method. At each aperture position, we collect a measurement in the form of S-parameters, where $S_{12}(f)$ is the frequency dependent phase and amplitude measurement of radiation emitted by port 2 and received by port 1. These measurements make up the vector $\mathbf{y}$ as described in Sec. III-E.

H. SAR Parameters

As seen in Figs. 1 and 2, the antennas move along the y axis (azimuth dimension) with a looking angle, α, measured from the z-axis (Nadir). The x-axis (ground range) is parallel to the imaging plane. For the 2D images, we move the antennas with the PR2 hand at an approximate height $h = 0.36$ m above the imaging scene. For all images shown here, we collect 151 frequency-dependent measurements as we step through the aperture positions, thus giving us information to reconstruct the image. We move the antennas a total linear distance of 0.6 m in the azimuth direction using a step size of 4 mm. With 151 points, each SAR imaging measurement takes approximately 12 minutes, limited by the MATLAB control of the PR2 and very slow data acquisition from the network analyzer (this would require only milliseconds with dedicated hardware). In addition, for each image, we take a background measurement in order to remove spurious reflections. When reconstructing the image, we coherently subtract the background from the measurement of the scene. The images we show here have been normalized and displayed on a log scale.

The step size of the moving aperture in SAR imaging must meet the Nyquist criterion to avoid spatial aliasing. The limit on the step size can be given by the azimuth resolution $\Delta y_{\max} = \frac{d_\mathrm{a}}{2} = 6.6$ mm with our antenna characteristics. Therefore, a step size of 4 mm will prevent aliasing in the azimuth domain. For both stripmap and spotlight mode, we use a bandwidth of 11.5 GHz, predicting a range resolution of $\delta_\mathrm{r} = 1.3$ cm.

In stripmap imaging, the length of our synthetic aperture is related to the physical antenna size in the azimuth dimension. Thus our predicted azimuth resolution is $\delta_{\mathrm{a,SAR}} = \frac{d_\mathrm{a}}{2} = 6.6$ mm. For these measurements we use a looking angle of $\alpha = 55^\circ$ and a squint angle of $\beta = 0^\circ$. The main lobe of the antennas is centered at a ground range of approximately $R_g = 0.5$ m from the plane of antenna motion. Our predicted ground range resolution is $\delta_\mathrm{gr} = 1.59$ cm. In spotlight mode, we move the squint angle from approximately -29° to 21° as we move the antennas along the linear path.

One potential source of error in our system is mismatch in the antenna positions for the background and image measurements due to limited repeatability of PR2 gripper position. These mismatches will result in noise (phantom points) in the reconstructed image.

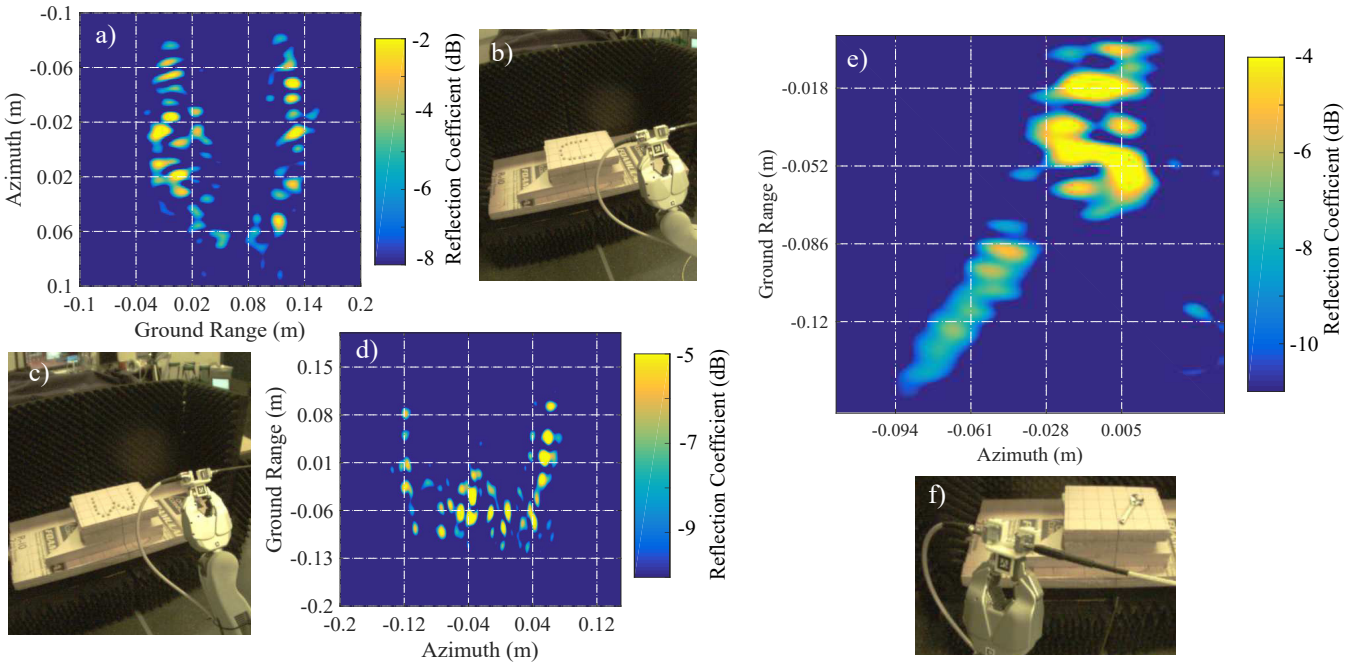

Fig. 4. SAR (a and d) and optical images (b and c) of a "U" and "W" made of 1/4"-20 nuts. (e) SAR image and (f) optical image of a metal wrench.

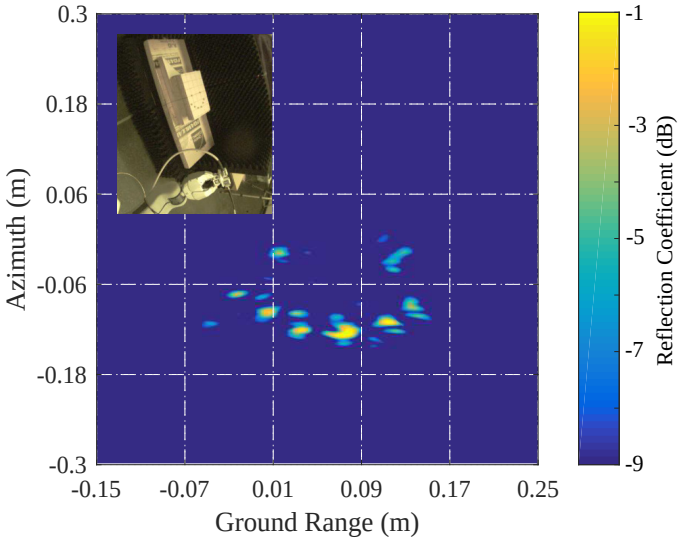

Fig. 5. SAR image and optical image (inset) of a smiley face made from 1/4"-20 nuts. All aperture position measurements were used in the reconstruction. Media file in supplemental information shows a buildup of the SAR image as aperture positions are added to the data set.

IV. Experimental Results

A. SAR Imaging System Resolution

Imaging a point source gives us the point spread function (PSF) of the SAR imaging system and thus a measure of the system resolution. Here we used a 1/4"-20 nut as an approximate point source. We took a PSF for both stripmap and spotlight imaging modalities, shown in Fig. 3. We can see from Fig. 3a that we obtain an approximate azimuth and ground range resolution of $\delta_{\mathrm{a,SAR}} = 1.45$ cm and $\delta_{\mathrm{gr}} = 1.52$ cm respectively.

It is clear from the figure that spotlight imaging garners increased azimuth resolution over stripmap imaging. From Fig. 3b, we see that spotlight SAR mode gives us an approximate azimuth and ground range resolution of $\delta_{\mathrm{a,SAR}} = 0.71$ cm and $\delta_{\mathrm{gr}} = 1.36$ cm.

B. SAR Images

In Fig. 4 we show several SAR images of different millimeter wave scenes. Fig. 4 shows SAR images (a and d) and optical images (b and c) of a U and W made of 1/4"-20 nuts. The optical images shown are taken from the camera mounted on the PR2. Fig. 4e shows an image of a metal wrench, where Fig. 4f shows the optical image, also taken from the PR2 camera.

In Fig. 5 we show an optical image (inset) and a SAR image of a smiley face made with 1/4"-20 nuts. This figure displays information from the last frame in a supplemental movie in which we show the build up of a SAR image from concurrent antenna measurements. In the movie, the left panel shows an optical image of the scene for that antenna position while the right panel shows the SAR image reconstruction using all measurements up to that point. We see the image of a smiley face made of 1/4"-20 nuts appear as we move through the aperture positions.

C. Imaging Concealed Objects

One of the clear advantages of using mmW systems is the ability to see through obstacles that optical imagers cannot penetrate. Not only could this include weather or darkness, but also seeing through materials such as paper, clothing, and cardboard. The potential for mmW imaging through opaque objects is widespread and ranges from security applications,

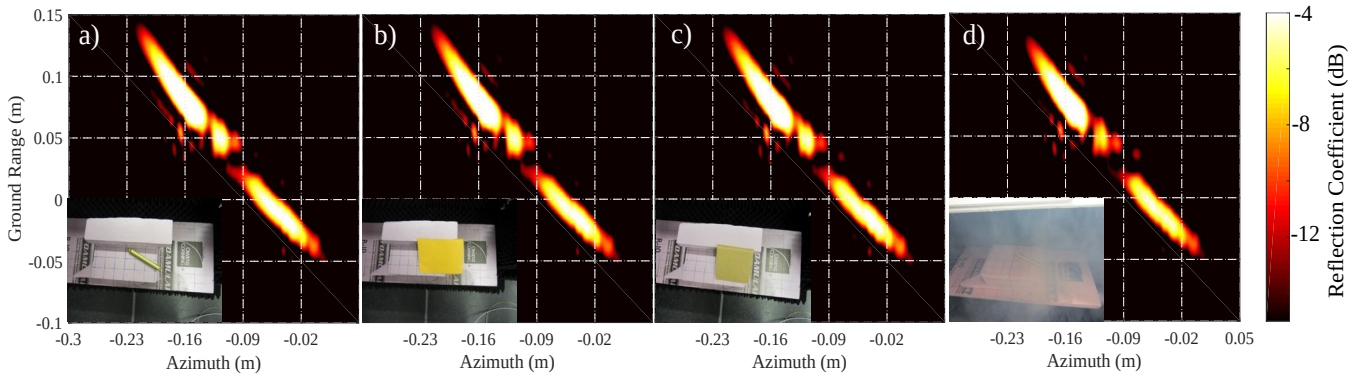

Fig. 6. SAR and optical images (insets) of a metal bar (a) un-obscured, (b) covered with one layer of an envelope, (c) covered with cardboard, and (d) obscured by fog.

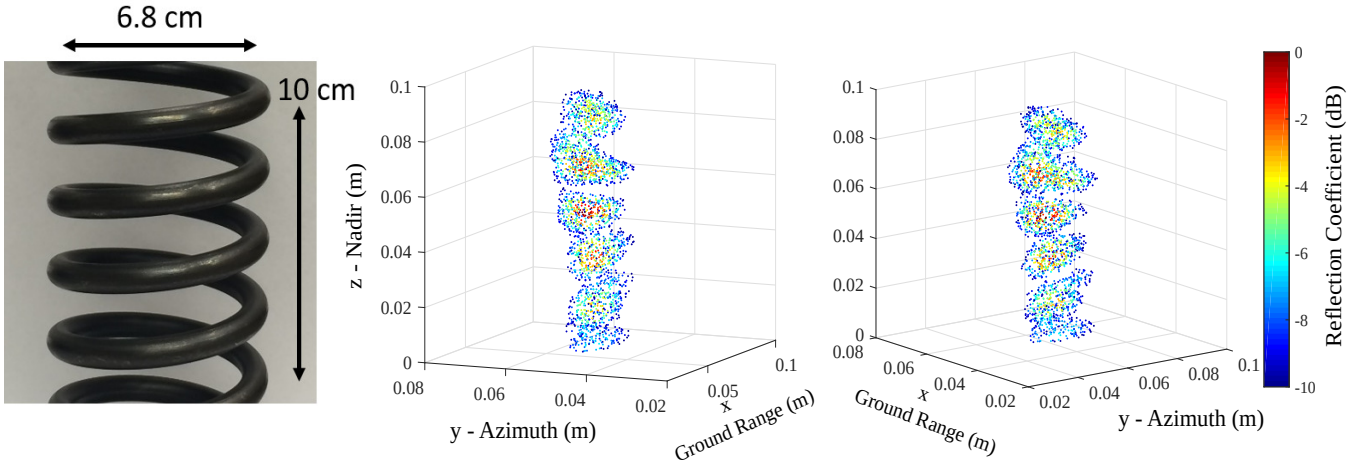

Fig. 7. 3D SAR image of a metal spring from 2 different viewpoint positions. Phase and amplitude were measured from the scene at points in a 2D grid to produce a 3D image.

operation in dangerous environments, to quality control of packaged goods.

In Fig. 6 we show several images of a metal bar (shown in the inset of Fig. 6a). The normal SAR image is shown in Fig. 6a. In the remaining panels, we image the same bar through several obstacles that deteriorate or completely destroy the optical image. The reconstructed SAR images are shown in (b) - (d) with a photograph of the scene shown in the inset of each one.

Fig. 6b shows the mmW image through a single layer of a manila envelope; Fig. 6c shows the metal bar through a layer of cardboard; Fig. 6d shows imaging through a layer of fog over the imaging plane.

We see that the mmW image is nearly identical from panel to panel, whereas the optical view of the bar is dramatically impaired or eliminated entirely.

D. 3D SAR Imaging

Up until now, we have been moving the antennas in a 1D scan, reconstructing a 2D scene. However, we can move the antennas in a 2D raster scan motion, allowing us to reconstruct a 3D scene. For these measurements, we move the antennas 0.4 m in y and z in a raster scan motion. In order to reduce the image acquisition time, we increase the step size to 7 mm, giving us 59 aperture points in each dimension, a total of 3481 aperture points.

In Fig. 7, we show a SAR image of a metal spring (photograph shown). Two different viewpoints of the 3D image are shown. From these images it can clearly be seen that we have reconstructed 3D components of the spring and can make out individual coils. A movie is shown in the supplemental information that rotates the scene around the z-axis.

V. Conclusion

In this work, we have shown that mmW SAR imaging has potential to complement measurements from optical sensors traditionally used by robots for perception and manipulation. A PR2 robot performed both 1D and a 2D scan of several objects with a set of bistatic horn antennas in order to recover 2D and 3D SAR images respectively. In comparing 1D scanning methodologies, the theoretical prediction that a spotlight scanning process can produce images with greater resolution than a stripmap technique was verified. Despite

imperfect replicability in the robot's end effector position between background and object image scans, compositions of point sources and real objects were successfully imaged even when the object is obscured by opaque materials or fog. Finally, a 2D radar scan was applied to a metal spring, producing a 3D point cloud that could provide useful geometric information in a robot manipulation scenario.

ACKNOWLEDGMENT

P.L. and J.R.S. are supported in part by the National Science Foundation under grant IIS-1427419. C.M.W., A.P.E., and M.S.R. acknowledge the support of the United States Government.

REFERENCES

[1] I. Cumming and F. H. Wong, *Digital processing of synthetic aperture radar data: algorithms and implementation*. Artech House, 2005.

[2] C. C. Chen, "Attenuation of electromagnetic radiation by haze, fog, clouds, and rain," DTIC Document, Tech. Rep., 1975.

[3] L. Gomes, "Hidden obstacles for Google's self-driving cars," 2014.

[4] J. J. Leonard and H. F. Durrant-Whyte, *Directed sonar sensing for mobile robot navigation*. Springer Science & Business Media, 2012, vol. 175.

[5] H. Surmann, K. Lingemann, A. Nuchter, and J. Hertzberg, "A 3D laser range finder for autonomous mobile robots," in *Proceedings of the 32nd International Symposium on Robotics*, 2001, pp. 153–158.

[6] R. El-laithy, J. Huang, and M. Yeh, "Study on the use of Microsoft Kinect for robotics applications," in *Position Location and Navigation Symposium (PLANS), 2012*, 2012, pp. 1280 – 1288.

[7] L. Robledo, M. Carrasco, , and D. Mery, "A survey of landmine detection technology," *International Journal of Remote Sensing*, vol. 30, no. 9, pp. 2399 – 2410, 2009.

[8] L. H. Nguyen, D. C. Wong, B. Stanton, and G. Smith, "Forward imaging for obstacle avoidance using ultrawideband synthetic aperture radar," in *AeroSense 2003*. International Society for Optics and Photonics, 2003, pp. 519–528.

[9] D. Langer, "An integrated MMW radar system for outdoor navigation," in *Proceedings IEEE International Conference on Robotics and Automation*, vol. 1. IEEE, 1996, pp. 417–422.

[10] F. Ali, G. Bauer, and M. Vossiek, "A rotating synthetic aperture radar imaging concept for robot navigation," *IEEE Transactions on Microwave Theory and Techniques*, vol. 62, no. 7, pp. 1545–1553, 2014.

[11] T. Deyle, M. S. Reynolds, and C. C. Kemp, "Finding and navigating to household objects with UHF RFID tags by optimizing RF signal strength," in *2014 IEEE/RSJ International Conference on Intelligent Robots and Systems (IROS 2014)*. IEEE, 2014, pp. 2579–2586.

[12] A. Marschall, T. Voigt, G. Li, U. Konigorski, and M. Vossiek, "Position control of a robot end-effector based on synthetic aperture wireless localization," in *2014 IEEE/RSJ International Conference on Intelligent Robots and Systems (IROS 2014)*. IEEE, 2014, pp. 163–168.

[13] A. Moreira, P. Prats-Iraola, M. Younis, G. Krieger, I. Hajnsek, and K. P. Papathanassiou, "A tutorial on synthetic aperture radar," *Geoscience and Remote Sensing Magazine, IEEE*, vol. 1, no. 1, pp. 6–43, 2013.

[14] A. Albert, *Regression and the Moore-Penrose Pseudoinverse*. Academic Press, New York, 1972.

[15] R. Solimene, I. Catapano, G. Gennarelli, A. Cuccaro, A. Dell'Aversano, and F. Soldovieri, "SAR imaging algorithms and some unconventional applications: A unified mathematical overview," *IEEE Signal Processing Magazine*, vol. 31, no. 4, pp. 90–98, July 2014.

[16] J. Nickolls, I. Buck, M. Garland, and K. Skadron, "Scalable parallel programming with CUDA," *Queue*, vol. 6, no. 2, pp. 40–53, Mar. 2008. [Online]. Available: http://doi.acm.org/10.1145/1365490.1365500

[17] *PR2 User Manual*, 321st ed., Willow Garage, 10 2012.

[18] "WR-42 standard gain horn antenna," http://www.pasternack.com.